Integration of Sentinel-1A/Landsat Imageries and Altimetry to Monitor the Mekong River Level

Kuan-Ting Liu[1] and Kuo-Hsin Tseng[2]
[1]Department of Civil Engineering, National Central University, No.300, Jhongda Rd., Jhongli City, Taoyuan, Taiwan
Email: 103322086@cc.ncu.edu.tw
[2] Center for Space and Remote Sensing Research (CSRSR), No.300,Jhongda Rd.,Jhongli City, Taoyuan, Taiwan
Email: khtseng@csrsr.ncu.edu.tw

KEY WORDS: Mekong River, Radar Altimetry, Landsat, Synthetic Aperture Radar

ABSTRACT:

This study proposed an alternative approach that combined multiple spaceborne sensors to investigate water level anomaly along the Mekong River potentially caused by the two dams in the upper stream, Xiaowan and Jinghong Dams. We examined water level (WL) dynamics in multiple river sections before and after the impoundment of these dams. Satellite missions including radar altimetry (RA, Envisat and Jason-2), satellite laser altimetry satellite (ICESat), Landsat-5/-7/-8 optical imageries and Sentinel-1A synthetic aperture radar (SAR) imageries were used to construct composite WL time series with enhanced spatial resolutions and substantially extended WL data records.

WL is considered as an important indicator of climatic impacts on water resources. Obtaining in-situ data could be expensive and time consuming for rivers/reservoirs in remote regions. As one of the most developed rivers in the world, Mekong River is in need of a monitoring system that could facilitate basin-scale management of water resources facing future climate change. In the study, a conversion function between altimetry WL and water extent from remote sensing images was first established for each dam and 6 checkpoints, and the combined long-term WL time series from Landsat/Sentinel-1A images were reconstructed for all checkpoints. 7 of 8 sites have R^2 between altimetry WL and Landsat water area (WA) measurements larger than 0.85. Finally, the impact of hydrologic dynamics caused by the impoundment of the dams is assessed. The root-mean-square error (RMSE) between estimated WL and in-situ data is at 2–5 m level at the dams, and about 1 m at downstream checkpoints. We concluded that the downstream river level is affected by a combined operation of these two dams in 2009-2015, which has decreased WL by 0.20 m $year^{-1}$ in wet seasons and increased WL by 0.35 m $year^{-1}$ in dry seasons.

1. Introduction

1.1 Study area

The Mekong River (MR) is the 7th-longest river in Asia. It is an important water source at Southeast Asia. The steep terrain in the upper MR is very suitable for hydropower construction. There are over 20 dams were built in the MR basin for store water and generate hydroelectricity. Some local news and organizations believed the dam construction has worsen the drought event at downstream area. However, due to the length and remoteness of the MR, it would be difficult to install and maintain adequate gauge stations to monitor the entire river. More importantly, other issues associated with economic/political restrictions/data latency would also result in data inaccessibility and unstable data quality in different countries. The feasibility to obtain timely and continuous observations at multiple sections along the river remains a challenge. These issues are highlighted, for example, in reports published by the Mekong River Commission, which is an inter-governmental organization that works with governments of Cambodia, Laos, Thailand and Vietnam, and creates a joint management of water resources and sustainable development. The data released by the MRC include gauge WL, discharge measurements, water quality, and drought information mainly in the lower Mekong watershed. However, because China is not a member of MRC, there is only one gauge located at Jinghong on the upper MR providing WL measurements of the dam. Moreover, the data only covered a limited period after the impoundment, which hinders the knowledge of downstream water availability. To monitor such an important yet poorly understood watershed, this study proposes to use timely satellite measurements at low-cost with reliable data quality.

In this study, we selected two dams located at the upper MR: Xiaowan and Jinghong Dam as our study sites. Furthermore, six downstream checkpoints were choose to analyze the impacts of dam construction. The location of study sites and checkpoints were shown in Figure 1. Some details about the dams were shown in Table 1.

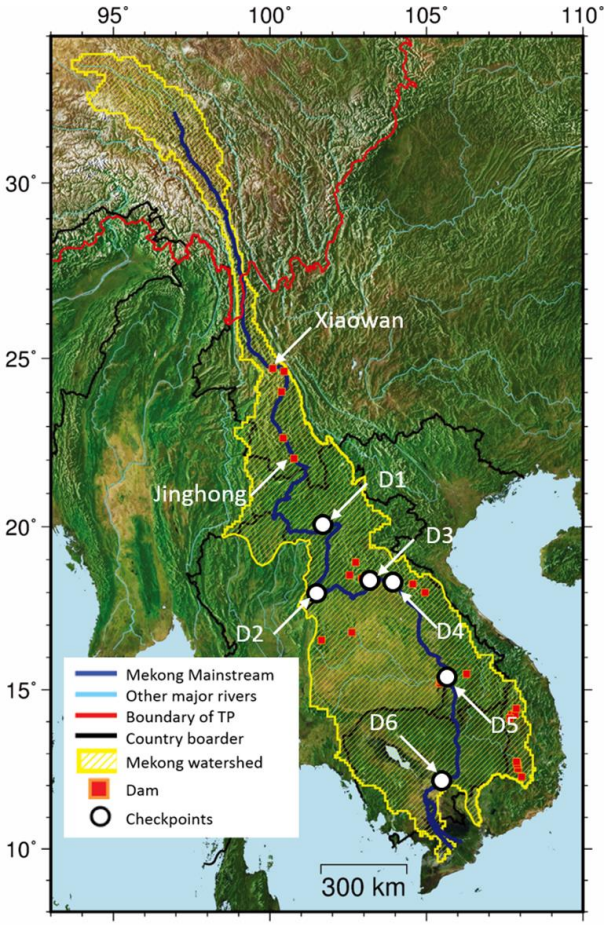

Figure 1. Locations of study sites: Xiaowan, Jinghong Dam and six checkpoints named D1-D6.

Table 1. Details about Xiaowan and Jinghong Dam.

	Xiaowan	**Jinghong**
Surface area (km^2)	11.33×10^4	14.91×10^4
Average annual inflow ($m^3 \cdot s^{-1}$)	1220	1840
Average annual discharge (m^3)	385×10^8	580×10^8
Normal water level (m)	1240	602
Downstream water level (m)	991	538.5
Total storage (m^3)	153.0×10^8	14.0×10^8
Dead storage (m^3)	43.5×10^8	8.1×10^8
Annual generation capacity (kW × h)	199.6×10^8	73.4×10^8

1.2 Satellite altimetry

Recent advances in geodetic satellite technology allow spaceborne sensors to be a feasible means to retrieve inland WL for adequately wide rivers. Satellite radar altimetry (RA) and laser altimetry (LA) was originally developed for ocean surface height and ice sheet observations (Fu, 1996). In this study, satellite RA and LA was used to retrieve WL information over study sites. New generation of altimetry satellites and the development of waveform retracking algorithm have improved the detectability and accuracy for inland WL observation. However, satellite RA is still limited by its long revisit periods, e.g., monthly sampling, or if the repeat period were reduced to 10 days, the cross-track spatial resolution would be coarser.

For satellite LA, the Ice, Cloud and land Elevation Satellite (ICESat), used laser photons to measure the height variation of ice sheet and water surface. With smaller footprint (~70 m in radius) compared with RA (3-5 km), it can observe narrow river channel without effects from other ground objects. But ICESat mission had just been operated in campaign mode with time span in 2003–2009. The ground track is not exactly repeat and temporal resolution is low, not enough to identify the seasonal WL variation.

1.3 Remote sensing images

We proposed an indirect method to convert extracted WA into WL measurements. By using Modified Normalized Difference Water Index (MNDWI) threshold classification, the WA information can be extracted from optical satellite images. In the study, Landsat-5/-7/-8 imageries covered from 2000 to 2016 were applied to extract WA. Landsat imageries have been shown powerful in characterizing the water-surface dynamics of inland water bodies. The satellites also provide the longest continuously remote sensing images, covered from 1972 (Landsat-1) until present (Landsat-7/-8). The acquired images are ideal for long-term environmental changes assessment.

On the other hand, backscattering coefficient of SAR images is also capable for WA classification without weather effects. Water surface will appear with relatively low backscatter compared with other objects, makes it very easy and robust to extract by radiometric thresholding. In this paper, all of the available Sentinel-1A SAR images

covered from 2014 until present were also used to extracted WA information. It is a space mission consisting of a constellation of two satellites (Sentilel-1A and Sentinel-1B) in the Global Monitoring for Environment and Security (GMES) mission, also known as Copernicus Programme. The main purpose of Sentinel-1A is to monitor land and ocean, providing C-band SAR images after decommissions of ERS-2 and Envisat.

2. Data and methodology

The workflow of the study was shown in Figure 2. The data includes multi-mission satellite RA (Envisat and Jason-2), LA measurements (ICESat), Landsat optical satellite imageries and Sentinel-1A SAR images.

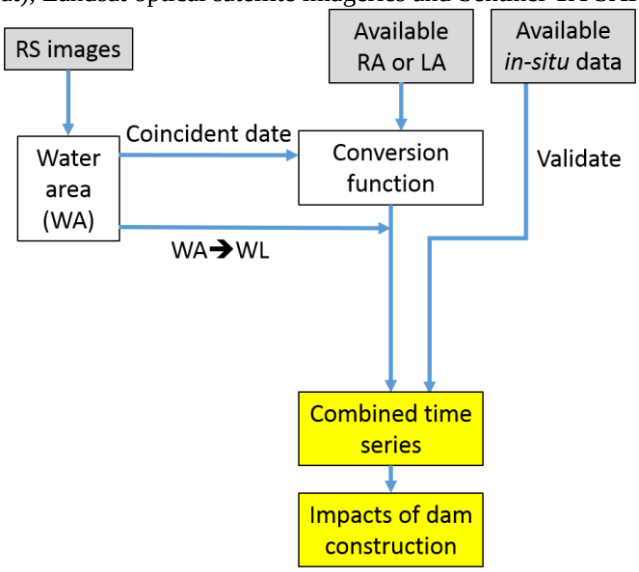

Figure 2. Workflow of the study.

2.1 Satellite altimetry

The Envisat high frequency (18 Hz) Ku-band data in the regular operation mode during 2002–2010 were used in this study. The altimetry data are stored in Sensor Geophysical Data Records (SGDRs) format for each cycle. The parameters include satellite position and timing, distance between satellite and surface and corrections. The Envisat SGDRs contained four different ranges calculated by standard waveform retracking algorithms (Kuo, 2011). For our study case, ICE-1 retracker is the most suitable algorithm to calculate range measurements for inland waterbody. Because it was originally developed for ice sheet observation purposes, and the waveform over inland waterbody with specular shape is similar to the return from ice sheet. Jinghong Dam finished in 2008 was able to be observed by Envisat pass #97, which has ~500 m water crossover. In order to ensure waveforms that were reflected from the water surface, a 15 dB backscattering coefficient (BC) threshold was set. The BC is used as an indicator of surface roughness, the higher the BC and flatter the surface in general. After applying correctional terms and waveform retracking adjustment, the altimetry WL time series near Jinghong Dam is created (Figure 3).

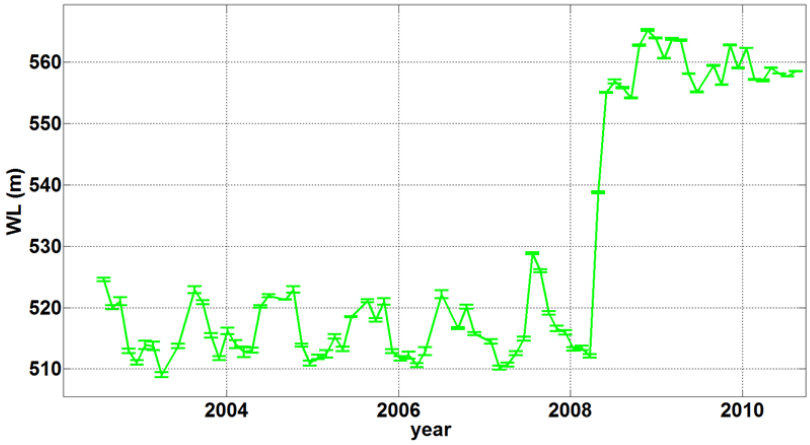

Figure 3. Envisat WL time series at Jinghong Dam.

The Ocean Surface Topography Mission (OSTM)/Jason-2 was launched in 2008. It is a follow-on mission to the TOPEX/Poseidon and Jason-1 missions. Jason-2 is equipped with a Ku/C-band dual-frequency radar altimeter that produces a sampling rate at 20 Hz, corresponding to a ground interval at 330 m. Xiaowan Dam can be observed by Jason-2, but Jinghong Dam has no crossovers within the reservoir. We used a similar 15 dB BC to ensure footprints were reflected from the water surface and generated satellite RA WL time series.

The Geoscience Laser Altimeter System (GLAS) on the ICESat, provides high accuracy laser altimetry measurements over the globe from 2003 to 2009. It measures the two-way travel time of laser pulses in wavelength of 1064 and 532 nm. It only worked in a 33-day to 56-day campaigns mostly in February–March/May–June/October–November during 2003–2009. By defining latitude and longitude range, the ICESat data inside the area can be extracted. We used a river channel in dry season as mask to further select the measurements returned from river surface (Figure 4). Next, we used visual inspection and standard deviation threshold to remove the outliers, the ICESat WL time series can thus be created (Figure 5). On account of its high accuracy and low temporal resolution, the available ICESat data was only used to combine with RS images and generate conversion function.

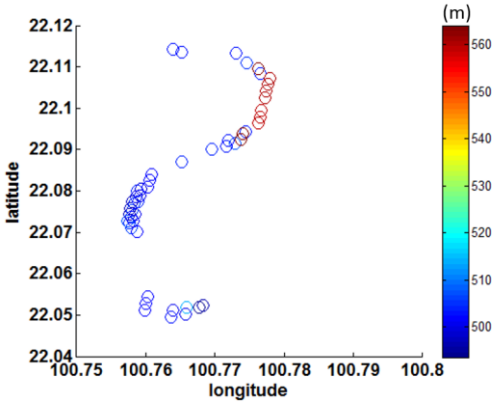

Figure 4. The available ICESat measurements inside river channel mask.

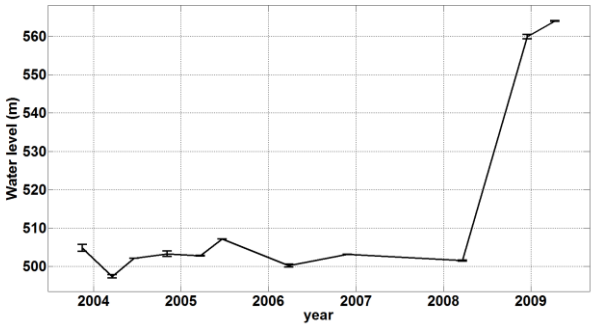

Figure 5. ICESat WL time series at Jinghong Dam

2.2 Optical images

All the available Level 1 image products were downloaded from U.S. Geological Survey (USGS) EarthExplorer website. The images were stored in GeoTiff format. For each study area, clear images without cloud cover over river channel were selected. The Digital Numbers (DNs) in each Landsat-5/-7 image were then converted into Top-of-Atmosphere (ToA) reflectance using Equations (1) and (2) (Chander, 2009). This procedure used the Earth-Sun geometry to define the reflectance measured by the satellite without performing correction for atmospheric effects. The ToA reflectance is sufficient in our study, because the analysis focused on the pattern of MNDWI, rather than absolute values. The MNDWI variability caused by water changes is much larger than the atmosphere effects.

$$L_\lambda = gain \times DN + bias \tag{1}$$

$$\rho_\lambda = (\pi \times L_\lambda \times d^2)/(ESUN_\lambda \times cos\theta s) \tag{2}$$

where L_λ is the cell value as radiance, DN is the cell value digital number, gain is the gain value for a specific band, bias is the bias value for a specific band, ρ_λ is the unitless plantary reflectance (ToA reflectance), d is the Earth–Sun distance in astronomical units, $ESUN_\lambda$ is the mean solar exoatmospheric irradiances, and θ_s is the solar zenith angle.

For Landsat-8 image, the conversion follows equations shown below:

$$\rho\lambda' = M_\rho Q_{cal} + A_\rho \tag{3}$$

where $\rho\lambda'$ is the ToA planetary reflectance without correction for solar angle, M_ρ is the band-specific multiplicative rescaling factor, A_ρ is the band-specific additive rescaling factor, and Q_{cal} is the quantized and calibrated standard product pixel values (DN). Furthermore, the ToA reflectance with a correction for the sun angle is:

$$\rho\lambda = \frac{\rho\lambda'}{sin(\theta_{SE})} \tag{4}$$

where $\rho\lambda$ is the ToA planetary reflectance and θ_{SE} is the local sun elevation angle.

The WA extraction for Landsat imageries can be achieved by several matured algorithms, such as single band estimation or supervised classification. In this study, a robust index called Modified Normalized Difference Water

Index (MNDWI) using green and mid-infrared bands was used to extract WA (Xu, 2006). In spectral analysis, waterbody has a strong reflectance in green band and substantial absorption in mid-infrared band. Water has values larger than zero in the MNDWI image (Figure 6), and other objects should be negative. The equation of MNDWI was shown below:

$$\text{MNDWI}_{\text{Landsat}} = \frac{Green - MIR}{Green + MIR} \quad (5)$$

The MNDWI threshold is slightly different for each study area. For TM/ETM+, the value 0.23 was set after inspecting several locations with false color images and testing different threshold values. Moreover, to avoid potential noise caused by clouds and terrain shadows, a river channel after impoundment plus a 5-pixel buffer area was used as a mask to further constrain the water extent. After the processing, the time series of extracted WA can thus be created. A sample of WA time series at Jinghong Dam was shown in Figure 6.

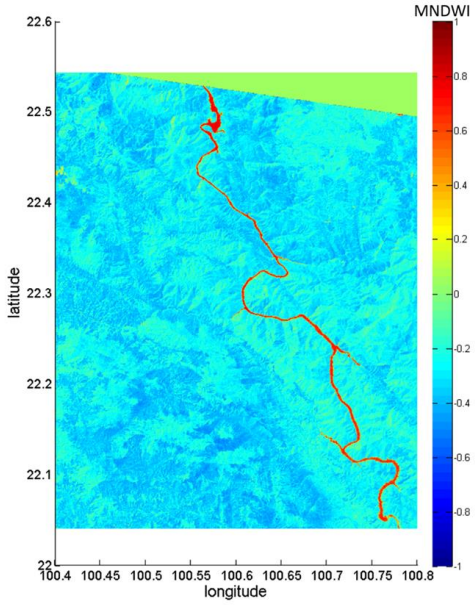

Figure 6. MNDWI image at Jinghong Dam.

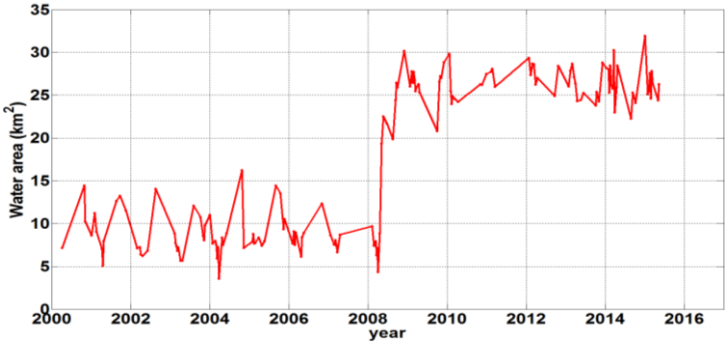

Figure 7. Landsat WA time series at Jinghong Dam.

2.3 SAR images

All of the available Sentinel-1A Interferometric Wide (IW) mode, VV polarization, High Resolution (HR), Level-1 SAR images covered from 2014 until present were used to extracted WA information. The data is available for free from Alaska Satellite Facility (ASF) data portal. The main purpose of Sentinel-1A is to monitor land and ocean, providing C-band SAR images after decommissions of ERS-2 and Envisat. With improved revisit period and coverage, it can provide higher temporal and spatial resolution images. The preprocessing tool for SAR images is called "Sentinel-1 Toolbox". The data preprocessing contained four steps: (1) Radiometric correction (2) Geometric correction (3) Speckle filtering and (4) image subset.

(1) The radiometric correction will remove the effects caused by slant range, incidence angle and illumination pattern of the antenna. After this step, the image can be converted from DN to Backscattering Coefficient (BC, σ). (2) Due to the characteristic of side looking, SAR images will be disturbed by terrain. The measured slant range need to convert into ground range and combined with DEM to generate images with correct location. We applied SRTM 1 sec digital elevation model in this step to correct the geometric distortion. (3) In order to perform better water classification result, a Lee filter is used to reduce these noise. It is a commonly used filter for SAR images. By using an eight-direction 5×5 moving window, Lee filter can keep the edge of the features and smooth the image. (4) Finally, all the images were cropped into the size of study area to speed up the processing. The sample of corrected and cropped SAR image is shown in Figure 8.

After the preprocessing steps, the WA in the SAR image has relatively lower BC values than other ground objects. So, we used two Gaussian distribution to fit the image histogram (Figure 8), and defined the BC threshold as Equation (6) to extract WA.

$$\text{Threshold} = \text{mean}_{\text{water}} + 1 \times \sigma_{\text{water}} \quad (6)$$

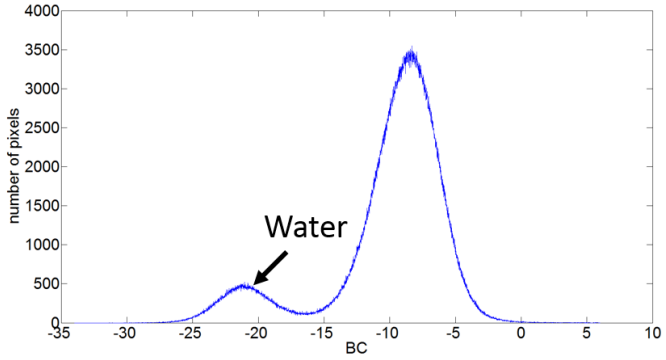

Figure 8. Histogram of the processed SAR image.

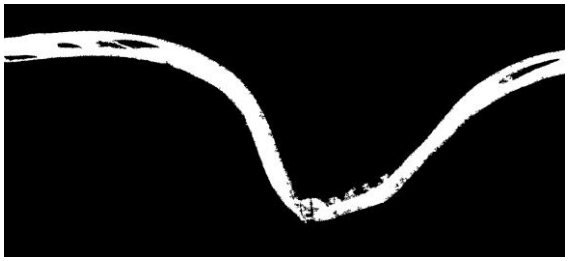

Figure 9. WA extracted from SAR image.

2.4 Conversion function between WL and WA

We first selected satellite images that were temporally coincident with altimetry measurements, and assumed the images acquired within ±3 days of altimetry data had the same WL for WA–WL conversion. For the selection of WL data for creating conversion function, available ICESat WL is prior to RA measurements because of its high accuracy. In all of these study sites, we used a linear function to fit the relationship between WA and WL. This contains uncertainty while the terrain slope is not a constant within the interval of water variation, and causing various non-linear WL–WA relationships correspond to different river sections. However, it's impossible to create accurate conversion function that fit every river section. Additionally, the analysis result work well without significant bias and are able to describe the WA-WL relationships for the selected Dams and checkpoints. All the R^2 between altimetry WL and RS-derived WA in most of the study sites are >0.85. The conversion functions for the dams and checkpoints are shown below:

$$WL_{Xiaowan}\ (m) = WA_{Xiaowan}\ (km^2) \times 1.611 + 1034 \quad (7)$$

$$WL_{Jinghong}\ (m) = WA_{Jinghong}\ (km^2) \times 2.549 + 491.3 \quad (8)$$

$$WL_{D1}\ (m) = WA_{D1}\ (km^2) \times 3.774 + 234.8 \quad (9)$$

$$WL_{D2}\ (m) = WA_{D2}\ (km^2) \times 0.3404 + 157.3 \quad (10)$$

$$WL_{D3}\ (m) = WA_{D3}\ (km^2) \times 1.408 + 94.44 \quad (11)$$

$$WL_{D4}\ (m) = WA_{D4}\ (km^2) \times 1.622 + 85.43 \quad (12)$$

$$WL_{D5}\ (m) = WA_{D5}\ (km^2) \times 2.317 + 58.26 \quad (13)$$

$$WL_{D6}\ (m) = WA_{D6}\ (km^2) \times 0.02144 - 9.41 \quad (14)$$

3. Results and validation

3.1 Combined WL time series

WL observed by combined altimetry and RS imageries in Xiaowan and Jinghong Dams are shown in Figure 10 and 11, respectively. With the same method, the WL time series at downstream checkpoints can also be created, a sample at D5 is shown in Figure 12. The red broken line in the panels is the measurement from Landsat optical images, the purple line is from Sentinel-1A SAR images. The blue line is from Jason-2, and the green line is from Envisat.

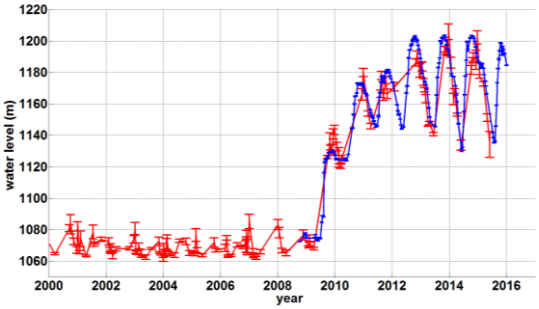

Figure 10. WL time series at Xiaowan Dam.

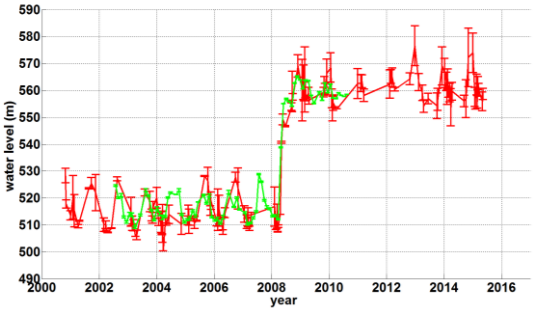

Figure 11. WL time series at Jinghong Dam.

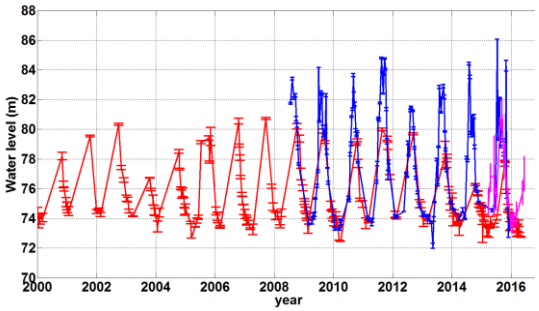

Figure 12. WL time series at D5.

3.2 Validation

Due to the lack of gauge data, we collected several WLs from local news during each stage of construction in Xiaowan and Jinghong Dam. The standard deviation of reported WL and estimated WL derived from a combination of altimetry and Landsat-derived measurements is 5.92 m during the five different time periods as shown in Table 2.

Table 2. Comparison between local WL information and estimated results of Xiaowan Dam.

	20 July 2009	**15 August 2009**	**1 August 2010**	**9 August 2011**	**15 November 2011**	**31 October 2012**
Local data (m)	1085	1126	1146	1173	1178	1200
Estimate results (m)	1084.78	1116.27	1144.46	1180.92	1181.68	1201.48

The local information of Jinghong Dam is obtained from Mekong River Commission website. Only a few corresponding values could be compared due to cloud cover in wet seasons (Table 3). The standard deviation of the difference between satellite-derived WL and ground truth is about 1.13 m at Jinghong Dam.

Table 3. Comparison between local WL information and estimated results of Xiaowan Dam.

	22 June 2009	**31 August 2009**	**5 October 2009**	**12 July 2010**	**16 August 2010**	**23 September 2012**
Gauge data (m)	555.77	560.36	557.05	556.91	556.88	557.45
Estimate results (m)	555.08	559.44	556.29	557.66	558.5	558.68

The WLs converted from WA data at D2, D4, D5, D6 were validated by available gauge measurements. We selected the in-situ data at the same date as RS time series and calculated RMSE, the validation results are shown in Table 4.

Table 4. The accuracy of estimated WL at checkpoints.

	D2	**D4**	**D5**	**D6**
Gauge	Chiang Khan	Paksane	Khong Chiam	Kompong Cham
Altimetry data	ICESat	Jason-2	Jason-2	ICESat
Accuracy (m)	0.77	1.00	1.03	0.89

3.3 Impact of Downstream Hydrologic Schemes

We calculated the mean WL in wet seasons (May–October) and dry seasons (January–April and November–December) for upstream and D1–D6 in each year. Then, applied a linear regression to derive the WL trend for each specified season. Because Jinghong Dam finished the impoundment in the first half of 2008, we only focused on the variation after rainy season of 2008. The results of each cross point, D1–D6, are shown in Figure 13 and 14. The uncertainty of WL estimate, as computed from 2-σ of data points in each season, is denoted as error bar in Figure 13 and 14.

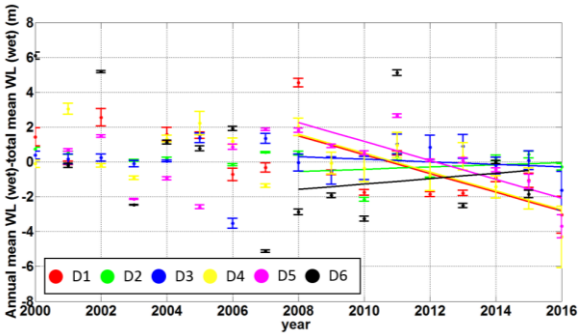

Figure 13. Decreasing wet season WL trend.

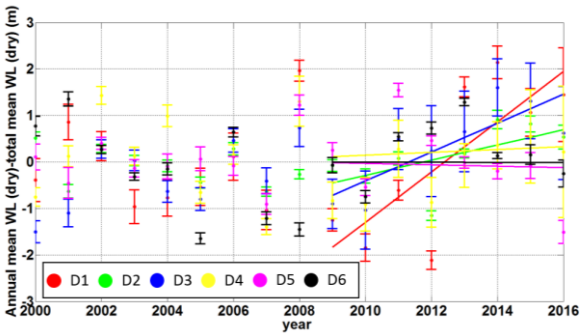

Figure 14. Increasing WL dry season trend.

For D1–D6, the average decreasing rate of maximum WL is about 0.32 m·year−1, and the average increasing rate of minimum WL is about 0.18 m·year−1. We conclude that the impoundment of these dams has reallocated water resources and changed river flow patterns compared with earlier years. Our results support the simulation in (Räsänen, 2012). Meanwhile, the pattern of shrinking water variability also seems to be less clear at point D6, which is distant from these dams. From the dry season WL variation rate in Figure 14, the closer to the dams, the larger increasing WL rate. It is suspected that along with the distance to the dams, water sources coming from other tributaries compensate the man-made adjustment and the pattern becomes insignificant.

4. Conclusion and future works

In this paper, we demonstrated an effective monitoring system to observe basin-scale WL variations by integrating data from multiple satellite observations. Two reservoirs and six river crossovers covered by altimetry, optical and radar RS satellites were analyzed to study the WL changes since the operations of dams in the upper Mekong basin. A decreasing trend in wet seasons and an increasing trend in dry seasons is identified by the combined time series. For now, the accuracy of estimated WL is limited to meter level, which might not suffice accurate hydrologic studies. However, this technique is promising because of its capability of densifying and extending the observations of WLs on remote rivers, lakes, and reservoirs, especially the monitoring of episodic signals such as dam water impoundment processes.

We investigated the hydrologic changes in the downstream of MR as a consequence of Dam operations upstream. Both RA and RS imageries can detect the impoundment of Xiaowan and Jinghong Dams and the seasonal variation of downstream points. However, some issues still need to be resolved or improved for further research. First, the extracted WA still contains errors due to terrain and cloud effects. In the future, it is preferred to establish a comprehensive decision tree for water delineation to exclude pixels with similar spectral behavior. Second, the conversion functions in current study were derived from first-order linear regressions, but the topography of the dams is not a linear structure. Formation of terrain should be taken into account to improve the estimates of empirical relationships between water extent and WL variations.

More altimetry satellites are expected to facilitate our future work on this topic. These new-generation satellites with improved designs of hardware will potentially outperform those historical missions. It is expected that the sampling rate can be increased, and the temporal coverage can be widened using higher temporal/spatial resolution satellite imageries, from platforms such as Formosat-2 and SPOT series of optical or synthetic aperture radar satellites. In summary, due to the availability of a variety of optical imageries, the monitoring system developed in this study can be a valuable tool for the monitoring of surface water variations at adequately fine spatial scales for water resources management.

5. References

Chander, G., Markham, B. L., & Helder, D. L. 2009. Summary of current radiometric calibration coefficients for Landsat MSS, TM, ETM+, and EO-1 ALI sensors. Remote sensing of environment, 113(5), 893-903.

Fu, L. L., & Smith, R. D. 1996. Global ocean circulation from satellite altimetry and high-resolution computer simulation. Bulletin of the American Meteorological Society, 77(11), 2625-2636.

Kuo, C. Y., & Kao, H. C. 2011. Retracked Jason-2 altimetry over small water bodies: Case study of Bajhang River, Taiwan. Marine Geodesy, 34(3-4), 382-392.

Räsänen, T. A., Koponen, J., Lauri, H., & Kummu, M. 2012. Downstream hydrological impacts of hydropower development in the Upper Mekong Basin.*Water Resources Management*, *26*(12), 3495-3513.

Xu, H. 2006. Modification of normalised difference water index (NDWI) to enhance open water features in remotely sensed imagery. International Journal of Remote Sensing, 27(14), 3025-3033.